Integrated electrically driven surface plasmon resonance device for biosensing applications

Alvaro Jimenez, Dominic Lepage, Jacques Beauvais, and Jan J. Dubowski[*]

Laboratoire Nanotechnologies Nanosystemes (LN2) - CNRS UMI-3463, Université de Sherbrooke, Interdisciplinary Institute for Technological Innovation (3IT), 3000 boul. de l'Université, Sherbrooke, QC J1K 0A5, Canada
[*]jan.j.dubowski@usherbrooke.ca

Abstract: Compact and portable surface plasmon resonance (SPR) biosensors of high sensitivities can be made through integration of discrete components in a single device. We report on a device comprising a vertical cavity light emitting diode (VLED) integrated with gold-based biosensing nanostructures fabricated atop its surface. Coupling of surface plasmon waves was achieved by the introduction of a spacer SiO_2 layer located between the light source and the functionalized Au thin film. The SPR signal was extracted in far field with a Au-based nanograting and detected using a custom designed hyperspectral imager. We discuss the performance of a VLED-based SPR device employed for detection of different concentration saltwater solutions.

©2015 Optical Society of America

OCIS codes: (280.1415) Biological sensing and sensors; (240.6680) Surface plasmons; (230.4170) Multilayers; (310.6860) Thin films, optical properties; (230.0250) Optoelectronics.

References and links

1. L. C. Clark, Jr. and C. Lyons, "Electrode systems for continuous monitoring in cardiovascular surgery," Ann. N. Y. Acad. Sci. **102**(1), 29–45 (1962).
2. J. H. T. Luong, K. B. Male, and J. D. Glennon, "Biosensor technology: technology push versus market pull," Biotechnol. Adv. **26**(5), 492–500 (2008).
3. A. P. F. Turner, "Biosensors: sense and sensibility," Chem. Soc. Rev. **42**(8), 3184–3196 (2013).
4. T. M. Chinowsky, J. G. Quinn, D. U. Bartholomew, R. Kaiser, and J. L. Elkind, "Performance of the Spreeta 2000 integrated surface plasmon resonance affinity sensor," Sens. Actuat, Biol. Chem. **91**, 266 (2003).
5. C. Thirstrup, M. Sakurai, T. Nakayama, and K. Stokbro, "Temperature suppression of STM-induced desorption of hydrogen on Si(100) surfaces," Surf. Sci. **424**(2-3), 329–334 (1999).
6. S. J. Kim, K. V. Gobi, H. Iwasaka, H. Tanaka, and N. Miura, "Novel miniature SPR immunosensor equipped with all-in-one multi-microchannel sensor chip for detecting low-molecular-weight analytes," Biosens. Bioelectron. **23**(5), 701–707 (2007).
7. Z. Geng, X. Ji, X. Lou, Q. Li, W. Wang, and Z. Li, "A surface plasmon resonance (SPR) sensor chip integrating prism array based on polymer microfabrication," in *2008 9th International Conference on Solid-State and Integrated-Circuit Technology (ICSICT)* (IEEE, 2008), pp. 2561–2564.
8. K. Nakamoto, R. Kurita, O. Niwa, T. Fujii, and M. Nishida, "Development of a mass-producible on-chip plasmonic nanohole array biosensor," Nanoscale **3**(12), 5067–5075 (2011).
9. L. Malic, K. Morton, L. Clime, and T. Veres, "All-thermoplastic nanoplasmonic microfluidic device for transmission SPR biosensing," Lab Chip **13**(5), 798–810 (2013).
10. M. M. W. Johnston, D. M. Wilson, K. S. Boosh, and J. Cramer, "Integrated optical computing: system-on-chip for surface plasmon resonance imaging," in *IEEE International Symposium on Circuits and Systems (ISCAS)*, **4**, 3483–3486 (IEEE, 2005).
11. R. Yan, S. P. Mestas, G. Yuan, R. Safaisini, D. S. Dandy, and K. L. Lear, "Label-free silicon photonic biosensor system with integrated detector array," Lab Chip **9**(15), 2163–2168 (2009).
12. M. Bora, K. Çelebi, J. Zuniga, C. Watson, K. M. Milaninia, and M. A. Baldo, "Near field detector for integrated surface plasmon resonance biosensor applications," Opt. Express **17**(1), 329–336 (2009).
13. D. Sammito, D. De Salvador, P. Zilio, G. Biasiol, T. Ongarello, M. Massari, G. Ruffato, M. Morpurgo, D. Silvestri, G. Maggioni, G. Bovo, M. Gaio, and F. Romanato, "Integrated architecture for the electrical detection of plasmonic resonances based on high electron mobility photo-transistors," Nanoscale **6**(3), 1390–1397 (2014).
14. D. Lepage and J. J. Dubowski, "Surface plasmon assisted photoluminescence in GaAs-AlGaAs quantum well microstructures," Appl. Phys. Lett. **91**(16), 163106 (2007).
15. D. Lepage and J. J. Dubowski, "Surface plasmon effects induced by uncollimated emission of semiconductor microstructures," Opt. Express **17**(12), 10411–10418 (2009).

16. D. Lepage, A. Jiménez, D. Carrier, J. Beauvais, and J. J. Dubowski, "Hyperspectral imaging of diffracted surface plasmons," Opt. Express **18**(26), 27327–27335 (2010).
17. D. Lepage, A. Jiménez, D. Carrier, and J. J. Dubowski, "Hyperspectral plasmonics," Proc. SPIE **7922**, 79220H (2011).
18. A. Jimenez, D. Lepage, J. Beauvais, and J. J. Dubowski, "Study of surface morphology and refractive index of dielectric and metallic films used for the fabrication of monolithically integrated surface plasmon resonance biosensing devices," Microelectron. Eng. **93**, 91–94 (2012).
19. D. Lepage, A. Jiménez, J. Beauvais, and J. J. Dubowski, "Conic hyperspectral dispersion mapping applied to semiconductor plasmonics," Light Sci. Appl. **1**(9), e28 (2012).
20. D. Lepage, A. Jiménez, J. Beauvais, and J. J. Dubowski, "Real-time detection of influenza A virus using semiconductor nanophotonics," Light Sci. Appl. **2**(4), e62 (2013).
21. D. D. Jenkins, "Refractive indices of solutions," Phys. Educ. **17**(2), 82–83 (1982).
22. W. M. Yunus and A. B. Rahman, "Refractive index of solutions at high concentrations," Appl. Opt. **27**(16), 3341–3343 (1988).

1. Introduction

The evolution of the optical and electronic technology has a tendency to consolidate discrete functions of systems in order to accommodate more functionality in less space. This approach allows reduction of the price, easier manipulation of devices and it makes complex systems available to consumers to execute much faster larger volumes tasks. Since the development of a first glucometer [1], applications for biosensing have followed this trend [2,3]. The exponential growth of biosensing research has the potential to improve the quality of life as well as create new markets.

Surface plasmon resonance (SPR) is one of the attractive techniques investigated extensively for the detection of interactions between proteins, antibodies with antigens and receptors with ligands. Advantages of the SPR technology include label-free detection, real time measurement of binding kinetics and relatively easy implementation for high throughput screening. The attractive characteristics of this technology contrasts with its low penetration into non-laboratory environment and other, non-biological, applications. The need for high quality discrete components and compromised sensitivity when attempting miniaturization have been the main obstacles for this technology to spread through consumer markets. Examples of miniaturized SPR devices based on the integration of discrete components have been discussed in literature [4–9]. A monolithically integrated device comprising an excitation source, a sensing component and an optical detector is required to further advance the miniaturization idea. A combination of sensing components with optical detection represents an approach discussed by some researchers [10–13]. In our experiments, we have focused on the integration of a light source with the sensing surface of an SPR device [14], and we presented the proof of concept of an SPR device with a single quantum well (QW) of a GaAs/AlGaAs microstructure that was pumped optically [15,16]. The QW photoluminescence (PL) was coupled with surface plasmon waves (SPW) in the near field of a thin film of Au. A SiO_2 spacer, separating semiconductor and metallic (Au) film was introduced to achieve efficient coupling, while the extraction of SPW in the far field was achieved using an Au nano-grating. The SPR signal was captured using a custom designed hyperspectral imager [16–18]. Working at 870 nm, the device was able to deliver a sensitivity of $1.5*10^{-6}$ RIU [19,20].

In this communication, we describe the concept and operation of a device comprising an electrically driven light source monolithically integrated with the sensing surface of an SPR device. The replacement of a single QW architecture with a commercial vertical cavity light emitting diode (VLED) allows controlling the irradiation conditions through an electrical bias.

2. Materials and methods

Figure 1(a) shows a schematic diagram of the investigated structure where a SiO_2 layer is located between the surface of a broadband emitting source and a thin metallic film of Au. For a given point of emission of the source, there is a simultaneous generation of all possible

wavelengths and wavevectors including those to generate SPR phenomena [$k_{x\text{-}SPR}(\lambda)$]. Generated SPW traveling along the dielectric/metal interfaces are diffracted with a Au grating fabricated atop of the functionalized metallic surface. Note that for the simplicity of the picture, the diagram of Fig. 1(a) illustrates propagation of k_{SPR} only in the direction of an *x*-axis. Figure 1(b) shows a 3D (k_x, k_y and energy E) extension of the SPR signal. As it can be seen, the resonance can be detected for any condition of $k_\parallel$ where $k_\parallel^2 = k_x^2 + k_y^2 = k_{SPR}^2$. For any wavelength, there is a dispersion relation of $\mathbf{k}_\parallel(\lambda)$ distributed in a 3D Fourier space. In the sketch of Fig. 1(b), a shaped cone called k_{ligth} is drawn as dictated by the microscope NA, the camera settings and the refractive index of the media under study. Only the SPR information inside of this cone is captured by the hyperspectral imager. Biochemical interactions on the Au surface investigated for biosensing applications lead to time-dependent modulations of SPR surfaces that can be tracked by the highly sensitive imaging system within the k_{ligth} cone.
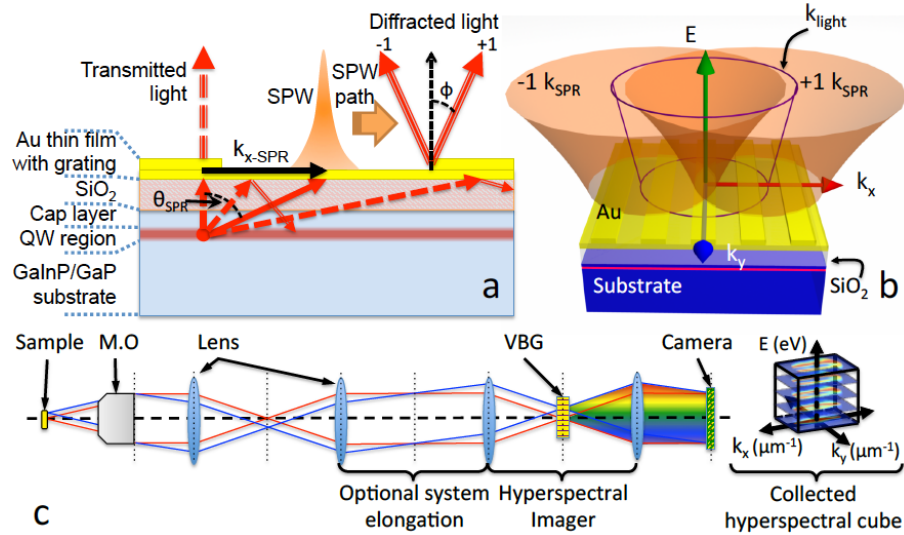

Fig. 1. Schematic diagram of an integrated SPR microstructure (a), the 3D propagation of the SPR signal generated by the system (b) and the hyperspectral setup for mapping of the SPR effect (c). For a given point of the source of light (a), there is a continuum of emissions covering all the range of wavevectors including the one ($k_{x\text{-}SPR}$) for generating a resonance between the top dielectric and metal film. The drawing shows how the SPW traveling over the dielectric/metal interface is diffracted in form of light for the first order by the grating (a). The sketch (b) shows the formation of the SPR signal in 3D space (k_x, k_y and E). Biosensing application is based on the following of the shift between the reference cone and the target, which has a different diameter. The hyperspectral imager (c) collects the information inside of the cone k_{ligth} (b). Optical signal from the sample is collected by M.O. and separated spectrally by a volume Bragg grating (VBG). The result is a 3D cube of intensity in Fourier space distributed by energy and wavevectors.

Figure 1(c) explains the principle of measuring the SPR signal in far field using a custom made hyperspectral imager. Optical information is collected by the microscope objective (M.O.) and a real image of the sample is formed in a volume Bragg grating (VBG) that spreads the wavevector information on the camera. Thus, the contrast images formed for different VBG positions can be deconvoluted into hyperspectral cubes.

A broadband non-collimated light source and the SPR architecture of our device imply the use of a hyperspectral imaging technology capable of delivering simultaneously information about SPR angles and spectral intensity of surface plasmons induced with the light source. However, this is not a working requirement. The system could very well be operated at a single wavelength, although such a reduction of the SPR bandwidth would impact overall sensitivity, as illustrated further in this manuscript. A large amount of data produced with the

hyperspectral imaging technique in a quasi-real time allows achieving stable signals characterized by attractive SNR values. Furthermore, in contrast with conventional methods of monitoring SPR signals, SPR tracking through microscopy is a more practical and affordable approach of wider applicability. We note that the current home build hyperspectral imaging system is a relatively bulky instrument, but it is not expected to be a limiting factor in the development of a technology of fully integrated miniaturised SPR devices as hand-held hyperspectral imaging cameras have emerged recently on the market, and their constant improvement, including sensitivity and resolution is expected to take place.

The investigated device employed a commercial VLED GaInP/GaP wafer emitting at 630 nm within a bandwidth of 12.4 nm. A 1 cm x 1 cm large samples were cut from the wafer, and designed to fabricate 25 emission zones for analysis, 1 mm x 1 mm each. Figure 2 shows an optical image of the device (a), and a sketch of the individual zone (b). The fabrication of samples included deposition of a SiO_2 layer with the required thickness, a photolithography step, etching of dielectric material and deposition of Ni/Au for the construction of the frames of emitting areas, deposition of thin layer of Au for the SPR coupling and e-beam lithography step for building the gratings. Alignment marks were necessary to facilitate the fabrication process. In order to extract the partial SPR profiles in the center of the image (inside of the cone of the light), the gratings are made with a periodicity of 450 nm and a ratio 1:1 between groove and ridge. The SiO_2 layers are 500 or 260 nm thick. The layer of Au and the grating where both 20 nm thick.
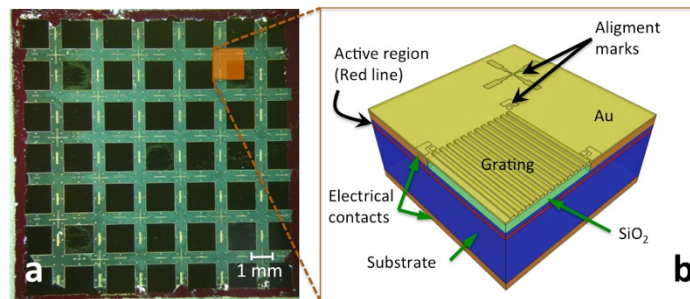

Fig. 2. Optical image of the sample with 25 SPR biosensing zones (a) and a sketch of the individual zone (b). The size of an emission area is of 1 mm x 1 mm. The detail of the structure (b) shows the contact areas, the SiO_2 layer and the grating on top of the functionalized surface. Alignment marks were made to facilitate the fabrication process involving photo and e-beam lithography.

Using a homemade software tool based on the RCWA method [14–17,20], we calculated the total output in the far field of the structures using SiO_2 layers of different thicknesses. It is well known that generation of SPR requires P-polarization across the metal/dielectric interface [15–20]. However, due to the nature of the excitation source used by our device, we found two interesting cases where the S-polarization mode of the optical signal has an effect on the total output. Figure 3(a) shows theoretical results at 625 nm wavelength for S-polarized (top) and P-polarized (bottom) modes using SiO_2 layers with two thicknesses: 500 nm (continuous line) and 260 nm (dashed line). For the sample with the thicker layer, we found the strong P-polarisation intensity, but there is also a significant presence of an S-polarized mode within the SiO_2, which is here considered as noise. In contrast to the SPR signal, the dispersion of this S-polarized mode changes very little with surface events. This mode creates a standing wave inside of the dielectric layer generating a strong SPR signal that mask the SPR information from the media under study. The thinner layer eliminates the interference generated by the S-polarization mode, but at the cost of a lower SPR intensity coupling.

The results of two sets of samples that were made with the mentioned thicknesses are shown in Fig. 3(b) (500 nm) and Fig. 3(c) (260 nm). These images show the measured light

intensity as a function of the wavelength and projected wavevector k_x. The amount of noise and interferences present in the sample with a 500 nm thick SiO_2 layer are evident. The two profile lines corresponding to the SPR signal are those having a V shape whose apex is expected at below 630 nm. All other profile lines correspond to the interference generated by the S-polarization mode, which they are so strong compared with the SPR signal under study, that the last one has been processed as noise. This phenomenon explains the non-uniformity in the edges of the SPR profiles for different wavelengths. The employment of a thinner layer of dielectric, as shown in Fig. 3(c), reduces the interference problem, leading to the SPR signal more suitable for biosensing applications. It can be seen that the investigated device architecture leads to overlapping of SPR profiles at $\lambda \geq 630$ nm.
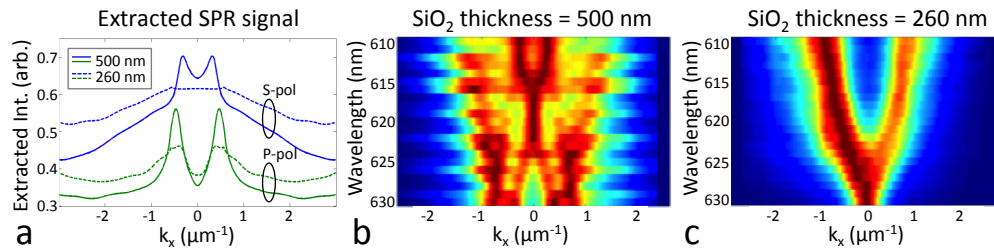

Fig. 3. Calculated (a) and measured total output SPR intensity for prototypes with 500 nm (b) and 260 nm (c) thick SiO_2 layers. A sample with the thicker layer of dielectric (b) shows strong interference from the S-polarization mode, making the SPR signal less defined. For the thinner layer of SiO_2, S-polarization modes are not coupled leaving the SPR signal much cleaner even if the P-polarization modes produce a weaker signal.

The response of fabricated devices to surface located reactions was carried out in a microfluidic chamber that was made in acrylonitrile butadiene styrene (ABS) using a 3D printing technique. The chamber was 5 mm tall, and it had an inverted cone shape with a 1 mm diameter apex and a 10 mm diameter base. This design permitted collecting SPR signal from individual sections (windows) of the device, without the interference of the signal originating from adjacent windows. The capacity of the chamber was 130 μL.

In the previous work [19,20], we discussed the application of both cubic and conic methods for real-time capturing the information concerning biosensing reactions. The cubic method has the advantage of extracting full information of the 3D space, as illustrated in Fig. 1(b). However, a time interval of 15 min between collecting consecutive data points makes this method impractical for tracking rapid biochemical reactions. In contrast, the conic method takes the information based on a particular cross-section of the SPR signal and images diffracted 'cones' of SPR in real-time each in less than 2 seconds. This allows for faster data acquisition, however at the expense of a partially lost resolution of the SPR signal. A relatively low S/N ratio of the SPR signal generated with the current VLED led us to work only with the cubic approach. Thus, we were not able to perform advanced biosensing experiments, although the principle of the operation of an electrically driven and integrated SPR device has been clearly demonstrated as discussed in this report.

3. Experimental procedure and results

Once the design and fabrication of the device was optimized for biosensing purposes, a series of experiments was carried out to investigate the device response to different saltwater solutions. For each concentration, the results were repeated at least three times. We used salt diluted in deionized (DI) water at 10, 20, 40 and 80 mg/mL. The sample chamber was flushed with DI water before the injection of an investigated solution and the solution was left stagnant during the 15 min acquisition time. Two runs were completed for the device exposed to a series of solutions with increasing concentrations, and one run was completed for the device exposed to the same series of solutions delivered in a reversed order. For the reference

purposes, we measured a response of the device to DI water at the beginning and the end of each run. Figure 4 explains the principle of measuring the shift of an SPR signal and it presents examples of SPR signals collected for samples exposed to different environments.
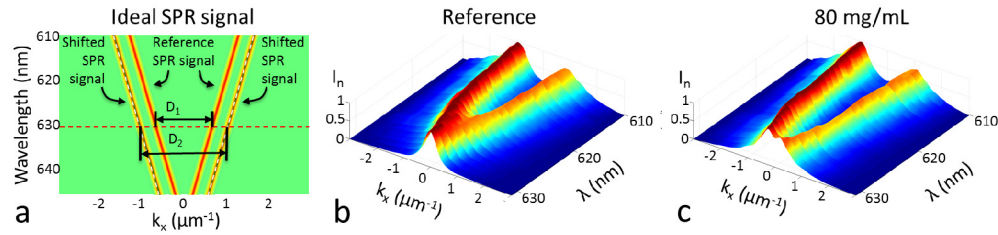

Fig. 4. The principle of measuring SPR shifts (a) and examples of SPR signals collected from samples exposed to deionized water (b) and a saline solution at 80 mg/mL (c). Changes in the SPR angle can be seen as increase of the separation distance between the two SPR profiles shown in (a) as D1 (reference) and D2 (saltwater solution). The thickness of SiO_2 dependent strength of some modes has resulted in overlapping of SPR profiles at $\lambda > 625$ nm, as seen in (b) and (c). However, the overall shift of the SPR profiles is evident as illustrated by the displacement of an apex towards higher wavelength values.

As it can be seen in Fig. 4(a), an increase of the refractive index of a medium surrounding the device results in the shift of the SPR maxima along the k_x axis (increasing angle of incidence for a given wavelength). Alternatively, this can be seen as a downward shift of the V-shape SPR plot. Due to the relatively broad SPR signal, it is difficult to notice the difference between details of the plots presented in Fig. 4(b) and 4(c), however, a downward shift of the SPR plot is clearly observed in Fig. 4(c). To determine the total shift, we created images corresponding to the mathematical differences in intensity per pixel for related plots, and we calculated the square root of the quadratic sums of accumulated shifts as a function of the wavelength.

Figure 5 shows the results of an SPR signal measured as a function of the wavelength (a) and time (b) for one of the investigated SPR devices exposed to different saline solutions. Numbers in both cases represent the concentration of salt diluted in water measured in mg/mL units. The notation of 00 indicates the use of pure water. Despite our interest in having recyclable samples, the samples with fresh surface were used in these experiments to reduce a possible chemical and/or mechanical modification of the SPR surface as well as contamination resulting from the exposure to different solutions.
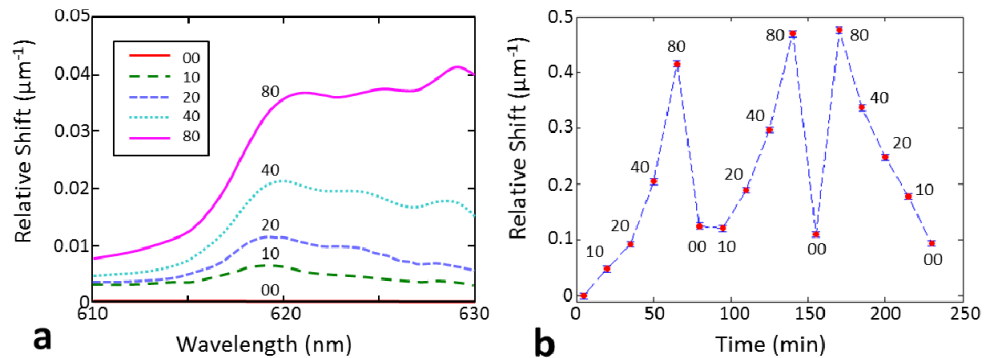

Fig. 5. Wavelength dependent (a) and time dependent (b) response (accumulated shift) of the SPR device to the presence of saline solutions at 10, 20 40 and 80 mg/mL. The best dynamic range of the SPR signal is observed at $\lambda \approx 619$ and 630 nm. An increase of the background level to near 0.10-0.12 μm^{-1} is observed in Fig. 5(b) following the injection of a saline solution.

The results obtained for a series of saline water samples allowed constructing a calibration curve as shown in Fig. 6. Open and full circles in Fig. 6(a) correspond to data collected at 624 nm and for the cumulated shift for all wavelengths, respectively. Based on the literature data taken at 632.8 nm [21,22], and our own data collected with a commercial nanoSPR system, the average values of RIU for different concentrations of saline water solution have been calculated and represented by a solid line in Fig. 6(b). This information allowed determining relative shift distances as a function of RI, as shown in Fig. 6(c). A linear fit of the 624 nm data and the all wavelength data, respectively, allowed determining related resolutions as 2.4 x 10^{-2} and 7.7 x 10^{-3} RIU/μm^{-1}, respectively. Thus, with an image resolution of 81.23 pixels/μm^{-1}, the estimated sensitivity of the measurements is 2.98 x 10^{-4} and 9.5 x 10^{-5} RIU for 624 nm and the complete information package, respectively.
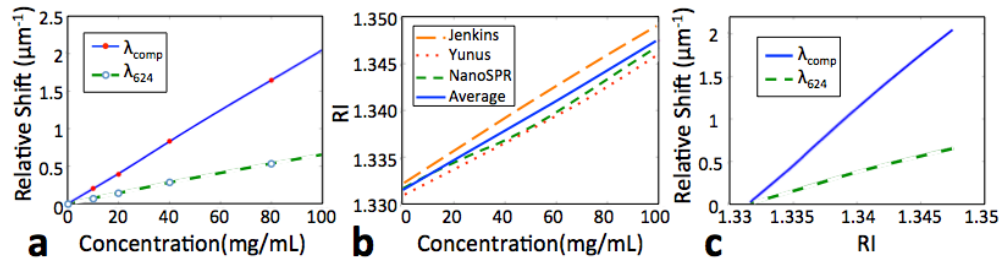

Fig. 6. Dependence of a relative SPR shift distance on the concentration of saline water solution for the 624 nm (open symbols) and accumulated for all wavelengths (full symbols) experiments (a). Average values of the refractive index (solid line) as a function of the concentration of saline water solution calculated based on the 632.8 nm literature data (dashed lines) [21, 22] and on the results obtained at 650 nm with a commercial NanoSPR instrument (dotted line) (b). The relative SPR shift distance of the investigated device calculated for 624 nm (dashed line) and for all wavelengths (solid line) in function of the refractive index (c).

4. Discussion

The wavelength dependent response of the SPR device (Fig. 5) has indicated that only the region between 615 - 630 nm provides a meaningful set of data. This limitation remains relatively unaffected even with the elimination of the contribution from the S-polarization mode, as suggested by the calculations. The fundamental reason for this behavior is related to the relatively narrow emission bandwidth of a VLED device employed in these experiments.

Some deterioration of the device sensitivity has been observed during the experiments involving saline water solutions. For example, Fig. 5(b) shows that, following the injection of the 10 and 20 mg/mL concentrates, the relative shift distance increased from 0 (DI water) to 0.1 μm^{-1}, and it remained almost unchanged at this level for the consecutive exposures to DI water. Meanwhile, the exposure to the 80 mg/mL concentrates resulted in a series of reproducible values of the relative shift distance at ~0.45 μm^{-1}. It is clear that the injection of DI water alone was not sufficient to remove the surface deposit of saline water, which was additionally enhanced by the nano-scale surface roughness of the investigated SPR chip.

The bulk sensitivity of the device was calculated using the same procedure as reported elsewhere [20] following only the cubic method. The sensitivities of 2.98 x 10^{-4} RIU and 9.5 x 10^{-5} RIU were found using a specific value of wavelength (624 nm) and an accumulated shift for all wavelengths, respectively. These values are almost one order inferior to those characterizing both a commercial system used as reference (1.0 x 10^{-5} RIU) and a recently reported SPR system with optically excited QWs using the same cubic method (4.8 x 10^{-5} RIU) [20]. The experiments carried out to characterize the VLED source have demonstrated that less than 10% of the optical power generated by this device participated in the coupling of SP waves. This is due to the significant absorption of light propagating at $k_{SPR}(\lambda)$ by the 700 nm thick AlInP layer used for the construction of the VLED device. With a typical 10%

efficiency of the light extracting nanograting, we estimate that less than 1% of the VLED output was measured by the microscope at k_{SPR}. Thus the S/N ratios from this device are much weaker than those previously observed from the PL-pumped SPR devices [20], consistent with the reduced sensitivities observed in the current experiment. Although the principle of an electrically driven SPR device monolithically integrated with a sensing surface has been demonstrated, the characteristics of the device did not allow studying biological reactions characterized by weak interactions. Thus, further experiments to demonstrate the use of this prototype in biosensing applications could not be realized. The future system should comprise an emitter capable of more efficient and direct coupling with SP waves, with the source emission bandwidth falling within the range of angles needed for the generation of SPR (e.g., $\pm$ 15 μm^{-1} in the region of 630 nm for the investigated here device). A large bandwidth of emission will generate better emission profiles in the hyperspectral space.

5. Conclusions

In a quest to develop an integrated electrically driven surface plasmon resonance device for biosensing applications, we have fabricated and investigated the operation of a device monolithically integrated with a light emitting diode. The potential advantage of such an approach is a significant miniaturization of a biosensing device that could be fabricated inexpensively with modern microfabrication technologies employing nanoimprint lithography, which is capable of an inexpensive delivery of nanometer period gratings over large surface area semiconductor wafers.

The device operation was tested in saline water solutions up to 80 mg/mL (n = 1.3329). The sensitivity of the device has been estimated at $\sim$3 x 10^{-4} RIU for a specific wavelength (624 nm) and $\sim$1 x 10^{-4} RIU for the accumulated shift induced by the investigated excitation bandwidth. We have established that the internal structure of the employed VLED device allowed less than 10% of the available optical power to pump the SPR signal. Also, the VLED device emitted in a relatively narrow bandwidth (FWHM) of the SPR exciting spectrum, which contributed to a relativity low contrast of S/N observed in the experiments. Fully integrated future SPR devices should also comprise a signal detection component, which could be addressed by designing a dedicated light-emitting diode microstructure with embedded photosensitive material.